

LETTER • **OPEN ACCESS**

Detecting global urban expansion over the last three decades using a fully convolutional network

To cite this article: Chunyang He *et al* 2019 *Environ. Res. Lett.* **14** 034008

View the [article online](#) for updates and enhancements.



LETTER

Detecting global urban expansion over the last three decades using a fully convolutional network

OPEN ACCESS

RECEIVED

30 September 2018

REVISED

1 December 2018

ACCEPTED FOR PUBLICATION


14 December 2018

PUBLISHED

11 March 2019

Original content from this work may be used under the terms of the [Creative Commons Attribution 3.0 licence](#).

Any further distribution of this work must maintain attribution to the author(s) and the title of the work, journal citation and DOI.

Chunyang He^{1,2}, Zhifeng Liu^{1,2,8} , Siyuan Gou^{1,2}, Qiaofeng Zhang³, Jinshui Zhang^{4,5,6} and Linlin Xu⁷

¹ Center for Human-Environment System Sustainability (CHESS), State Key Laboratory of Earth Surface Processes and Resource Ecology (ESPRE), Faculty of Geographical Science, Beijing Normal University, Beijing 100875, People's Republic of China

² School of Natural Resources, Faculty of Geographical Science, Beijing Normal University, Beijing 100875, People's Republic of China

³ Department of Geosciences, Murray State University, KY 42071, United States of America

⁴ ESPRE, Beijing Normal University, Beijing 100875, People's Republic of China

⁵ Beijing Engineering Research Center for Global Land Remote Sensing Products, Faculty of Geographical Science, Beijing Normal University, Beijing 100875, People's Republic of China

⁶ Institute of Remote Sensing Science and Engineering, Faculty of Geographical Science, Beijing Normal University, Beijing 100875, People's Republic of China

⁷ School of Land Science and Technology, China University of Geosciences, Beijing 100083, People's Republic of China

⁸ Author to whom any correspondence should be addressed.

E-mail: zhifeng.liu@bnu.edu.cn

Keywords: fully convolutional network, global urban expansion, deep learning, nighttime light data, vegetation index, land surface temperature

Abstract

The effective detection of global urban expansion is the basis of understanding urban sustainability. We propose a fully convolutional network (FCN) and employ it to detect global urban expansion from 1992–2016. We found that the global urban land area increased from 274.7 thousand km²–621.1 thousand km², which is an increase of 346.4 thousand km² and a growth by 1.3 times. The results display a relatively high accuracy with an average kappa index of 0.5, which is 0.3 higher than those of existing global urban expansion datasets. Three major advantages of the proposed FCN contribute to the improved accuracy, including the integration of multi-source remotely sensed data, the combination of features at multiple scales, and the ability to address the lack of training samples for historical urban land. Thus, the proposed FCN has great potential to effectively detect global urban expansion.

1. Introduction

Urban expansion represents the transformation of non-urban land to urban land, which results in increases of the areas of cities (Seto *et al* 2011). In the context of rapid urban population growth and socio-economic development, the world has undergone large-scale urban expansion (Wu 2014, Angel *et al* 2016). Between 2000–2010, the global urban land area increased from 0.6 million km² to 0.7–0.9 million km², and these values reflect growth rates of 18.1%–44.2% (Angel *et al* 2011). By 2050, the global urban land area is projected to expand to 1.2–3.1 million km², which is 1.6–3.6 times the global urban land area in 2010 (Angel *et al* 2011). Global urban expansion has caused many ecological and environmental issues, such as losses of biodiversity, increases in carbon emissions, water scarcity, regional warming, and

environmental pollution (Grimm *et al* 2008, McDonald *et al* 2008, 2013, Seto *et al* 2012, Liu *et al* 2016b, Bren d'Amour *et al* 2017, van Vliet *et al* 2017). To evaluate such effects of urban expansion, reliable information on global urban expansion is indispensable (Seto *et al* 2011, Liu *et al* 2014). Thus, how to effectively detect global urban expansion has become a crucial issue in understanding urban sustainability (Zhang and Seto 2011, Wu 2014, Angel *et al* 2016).

At present, data on global urban expansion come from eight widely referenced sources (table 1). These data represent global urban expansion during six periods, 10000 BC–2016, 1975–2014/2015, 1990–2010, 1992–2015, 2000–2010 and 2010–2017 (table 1). Of these sources, the HYDE describes global urban expansion from 10000 BC–2016 (Klein Goldwijk *et al* 2010). The GHS data reveal global urban expansion from 1975–2014/2015 (Pesaresi *et al* 2013, 2016). The

MGIS data represent global urban expansion from 1990–2010 (Liu *et al* 2018). The global land cover data derived from the ESACCI describe global urban expansion from 1992–2015 (UCL-Geomatics 2017). The GLC30 dataset and the IMPSA dataset represent global urban expansion between 2000–2010 (Elvidge *et al* 2007, Chen *et al* 2015). The FROM-GLC data reveal global urban expansion from 2010–2017 (Gong *et al* 2013). These data have been widely used to understand the ecological and environmental effects of urban expansion across the world (Klein Goldwijk *et al* 2010, Pesaresi *et al* 2013, 2016, UCL-Geomatics 2017). However, the HYDE data have a low resolution of 10 km and thus do not provide adequate spatial information. The GHS data, the FROM-GLC data and the ESACCI data are limited by their low accuracy; the kappa value of the GHS data is approximately 0.3 (Pesaresi *et al* 2016), the overall accuracy (OA) of the FROM-GLC data is approximately 60% (Gong *et al* 2013), and the producer's accuracy of the ESACCI data is approximately 51% (UCL-Geomatics 2017). The MGIS, GLC30 and IMPSA datasets lack information on global urban expansion after 2010. Thus, developing effective methods of detecting global urban expansion is still worthwhile (Esch *et al* 2017).

Fully convolutional network (FCN)-based methods provide a novel approach to the detection of global urban expansion. The FCN is a deep learning structure that employs the 'pixel-to-pixel' image recognition mode developed by Long *et al* (2015) on the basis of the convolutional neural network (CNN). FCN-based models inherit the basic structure of CNN; their primary components include convolutional layers, pooling layers, activation layers, and concatenation layers (Long *et al* 2015). Of these layers, convolutional layers can identify the local features of images; pooling layers compress numerous features to extract the main features; activation layers effectively express nonlinear features; and concatenation layers integrate features over multiple scales (LeCun *et al* 1990, 1998, 2015, Szegedy *et al* 2014). Through transmitting information between multiple convolutional layers, pooling layers, activation layers and concatenation layers, FCNs effectively integrate remote sensing data from multiple sources and features over multiple scales to identify objects accurately (Chen *et al* 2017, Yang *et al* 2017). Furthermore, FCNs have the ability to transfer learning, which enables the extraction of dynamic information using parameters obtained from training samples in a single period. Recently, researchers have started to use FCN-based methods to detect urban land at different scales. For example, Maggiori *et al* (2016) employed FCN-based methods to quantify the patterns of urban land in Boston, United States, whereas Fu *et al* (2017) applied FCN-based methods to extract urban land in the north-eastern parts of Beijing, China. However, FCNs have not been used to detect global urban expansion.

Our objective is to propose a new FCN to detect global urban expansion from 1992 to 2016 at 1 km. To

achieve this goal, we first develop an FCN to integrate remotely sensed data from multiple sources effectively. We then use the proposed method to extract the global urban land in 1992, 1996, 2000, 2006, 2010, and 2016 using nighttime light (NTL) data, normalized difference vegetation index (NDVI) data, and land surface temperature (LST) data. Our method provides an effective means of detecting global urban expansion over large scales.

2. Study area and data

2.1. Study area

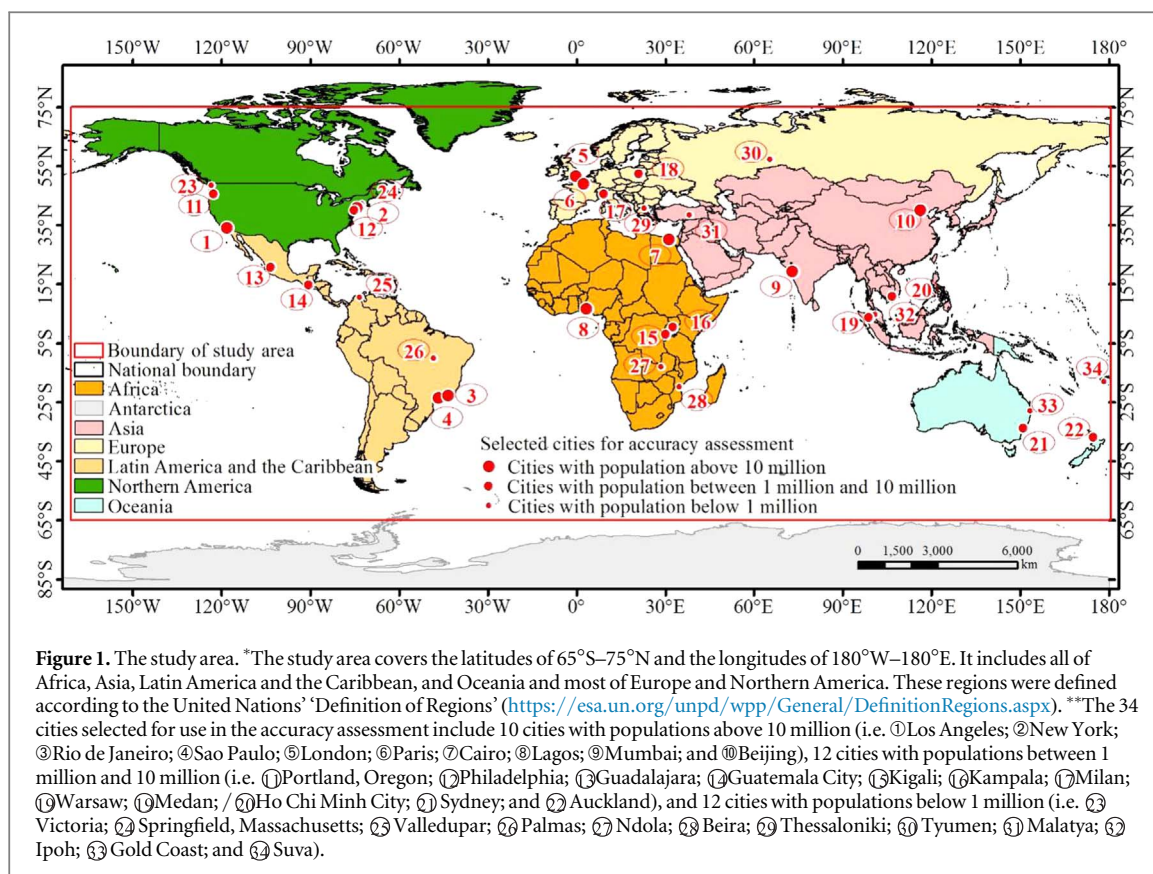
Our study area is located from 65°S–75°N latitude worldwide, identical to the areal coverage of the NTL data (figure 1). This zone contains 0.13 billion km² of land surface area and accounts for 89.26% of the global land surface area. It includes all of Asia, Africa, Latin America and the Caribbean, and Oceania, and most of Europe and Northern America (figure 1).

2.2. Data

This study makes use of several data sources with global coverage, specifically the NTL, NDVI, and LST data mentioned above, to detect urban expansion. The 500 m Moderate Resolution Imaging Spectroradiometer (MODIS) Urban Land Cover (MOD500) data are used to select the training samples. Urban population statistics, Landsat images, and existing GHS data and the ESACCI global land cover data were also obtained.

The NTL data were obtained from the NOAA/NGDC (<http://ngdc.noaa.gov/eog>, accessed 20 September 2017). These data were collected by the Defense Meteorological Satellite Program's Operational Linescan System (DMSP-OLS) and include uncalibrated NTL data acquired in 1992 and radiance-calibrated NTL data from 1996, 2000, 2006, and 2010 at a resolution of 1 km. The monthly NTL data from 2016 at a resolution of 742 m acquired by the Suomi National Polar-orbiting Partnership's Visible Infrared Imaging Radiometer Suite (NPP-VIIRS) were also obtained. The approach introduced by Elvidge *et al* (2009) is applied to intercalibrate the uncalibrated NTL data collected in 1992 to improve their continuity and comparability, and the approach developed by Elvidge *et al* (2013) is performed to produce the annual mean value composite of the 2016 VIIRS NTL data. To reduce the influence of gas flares, we follow Zhou *et al* (2014, 2015) to exclude gas flare pixels from the NTL data using the gas flare mask obtained from NOAA/NGDC.

The NDVI data include the MODIS NDVI data for 2000, 2006, 2010, and 2016 and the NOAA-AVHRR NDVI data for 1992 and 1996 at a resolution of 1 km. The MODIS NDVI data were obtained from the MODIS 16 d composite products (<http://ladsweb.nascom.nasa.gov>, accessed 20 September 2017). The NOAA-AVHRR NDVI data were obtained from the USGS website (<https://lta.cr.usgs.gov/NDVI>, accessed



20 September 2017). Using the maximum value composite (MVC) approach introduced by Holben (1986), an annual MVC of the NDVI data for each year is produced to reduce cloud contamination.

The LST data in 2000, 2006, 2010, and 2016 at a resolution of 1 km are derived from the MODIS eight-day composite product (MOD11A2) (<http://ladsweb.nascom.nasa.gov>, accessed 20 September 2017). The nighttime LST data in this product are used because the LST in nighttime generally has better performance for distinguishing between urban and non-urban land (Buyantuyev and Wu 2010, Zakšek and Oštir 2012). Consistent with Mildrexler *et al* (2009), an annual MVC of the LST data for each year is also produced.

The MOD500 data used to select training samples were obtained from the Center for Sustainability and the Global Environment at the University of Wisconsin-Madison (<http://www.sage.wisc.edu/>, accessed 20 September 2017). The MOD500 data are produced through supervised classification of MODIS multi-spectral data circa 2001 (Schneider *et al* 2009, 2010). The data have an OA of 93%, which is a relatively accurate representation of the global urban land area (Schneider *et al* 2009, 2010). All of the NTL, NDVI, LST, and MOD500 data are resampled to a spatial resolution of 1 km. In addition, all of the data layers are geometrically corrected with reference to the MOD500 data.

In addition, the statistical data on the global urban population used for the accuracy assessment were obtained from the World Urbanization Prospects

published by the United Nations Department of Economic and Social Affairs (2015) (<https://esa.un.org/unpd/wup/>, accessed 20 September 2017). The Landsat images were obtained from the USGS (<http://glovis.usgs.gov.com>, accessed 20 September 2017). The built-up grid and settlement grid of the GHS Layer were obtained from the European Commission Joint Research Center (<http://ghslys.jrc.ec.europa.eu/>, accessed 20 September 2017). Finally, the ESACCI data were obtained from the European Space Agency (<http://maps.elie.ucl.ac.be/CCI/viewer/index.php>, accessed 20 September 2017).

3. Methods

3.1. Developing the FCN

Following the basic FCN framework presented by Long *et al* (2015), we develop a new FCN for detecting global urban expansion (figure 2). The FCN mainly includes one input layer, one pooling layer, three convolutional layers, one concatenation layer, and one output layer, and each convolutional layer follows an activation layer (figure 2(b)). The input layer is used to integrate the NTL, NDVI, and LST data to provide both socioeconomic and physical information. Longitudes and latitudes are also entered to provide information on the location of urban land. The convolutional and pooling layers are used to obtain feature information from the data at the pixel, neighborhood and urban region scales. The

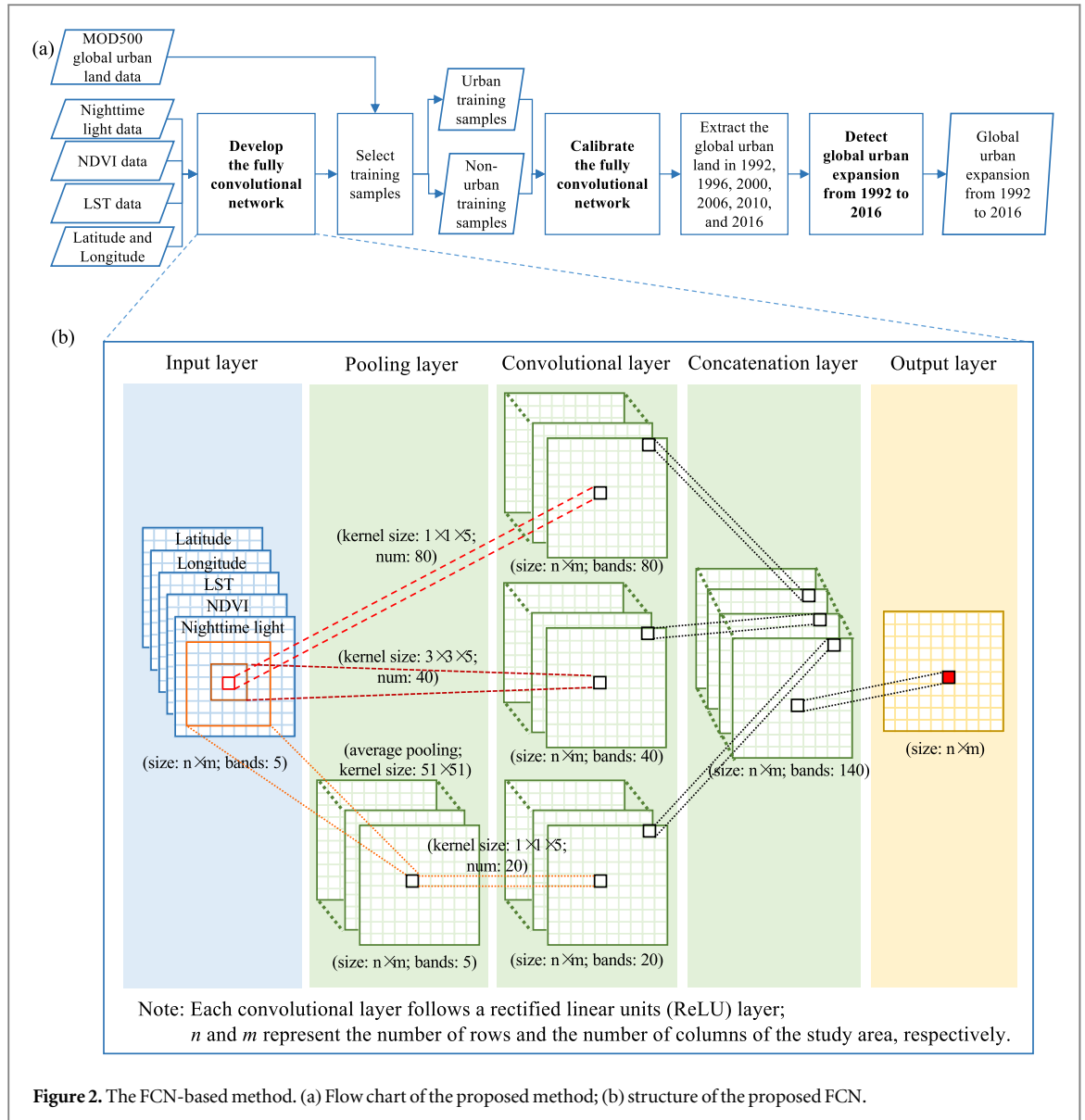


Figure 2. The FCN-based method. (a) Flow chart of the proposed method; (b) structure of the proposed FCN.

concatenation layer is used to integrate the feature information at the three scales to identify urban land (figure 2(b)).

When extracting global urban land in 2000 and after, the input layers include five bands, specifically NTL, NDVI, LST, longitude, and latitude. However, when extracting urban land for 1992 and 1996, the input layer includes only four bands, specifically NTL, NDVI, longitude, and latitude. That is, the MODIS LST data are unavailable.

The three convolutional layers and the pooling layer employ different numbers and sizes of convolutional kernels to obtain information on urban land at three scales of pixel, neighborhood and urban region. Both the numbers and sizes of the convolutional kernels are determined following previous studies and trial-and-error procedures (LeCun *et al* 1990, Szegedy *et al* 2014, Long *et al* 2015).

The first convolutional layer contains 80 convolutional kernels with a size of 1×1 pixel and is used to obtain information at the pixel scale. Its relationship

with the input layer can be represented by the equation (1):

$$Conv_{i,j}^1 = \sum_I^{N_0} (W_{I,i}^1 \cdot Input_{I,j}) + Bias_i^1, \quad (1)$$

where $Conv_{i,j}^1$ and $Input_{I,j}$ denote the DN values in the first convolution layer and the input layer respectively; i and I indicate the band; j indicates the pixel; $W_{I,i}^1$ is the weight of this convolution layer; $Bias_i^1$ is the bias; and N_0 is the number of bands.

The second convolutional layer contains 40 convolutional kernels with a size of 3×3 pixels and is used to obtain information at the neighborhood scale. Its relationship with the input layer can be represented by the equation (2):

$$Conv_{i,j}^2 = \sum_I^{N_0} \sum_d^{K_1 \times K_1} (W_{I,i,d}^2 \cdot Input_{I,j,d}) + Bias_i^2, \quad (2)$$

where $Conv_{i,j}^2$ and $Input_{I,j,d}$ denote the DN values in the second convolution layer and the input layer respectively; d indicates the pixel in the neighborhood

Table 1. Overview of the existing data on global urban expansion.

Time period	Spatial resolution	Name of dataset	Abbreviation	Urban land definition	Method	Data source	Reference
10000 BC-2016	10 km	History Database of the Global Environment	HYDE	Built-up area	Urban population density-based statistical model	DISCover map, GLC2000, Landsat population data, and Demography data	(Klein Goldwijk <i>et al</i> 2010)
1975–2014/ 2015	38 m/ 25 m/ 1 km	Built-up grid of the Global Human Settlement Layer	GHS built-up	Built-up area	Symbolic machine learning	Landsat images	(Pesaresi <i>et al</i> 2013, 2016)
	1 km	Global Human Settlement layer's settlement grid	GHS SMOD	Urban centers / urban clusters	REGIO-OECD 'degree of urbanization' model	GHS built-up and population data from CIESIN GPW v4	(Pesaresi <i>et al</i> 2013, 2016)
1990–2010	30 m	Multi-temporal Global Impervious Surface	MGIS	Impervious surface	Normalized urban areas composite index	Landsat images	(Liu <i>et al</i> 2018)
1992–2015	300 m	Climate Change Initiative-land cover	ESACCI	Built-up area	Unsupervised classification and change detection	Global urban footprint, GHS built-up, MERIS images, AVHRR images, SPOT-VGT images and PROBA-V images	(UCL-Geomatics, 2017)
2000–2010	30 m	Global Land Cover at 30 m resolution	GLC30	Impervious surface	Pixel-object knowledge-based classification and visual interpretation	Landsat images and HJ-1 images	(Chen <i>et al</i> 2015)
	1 km	Global Impervious Surfaces	IMPSA	Impervious surface	Linear regression model	DMSP-OLS nighttime light data and Landsat population data	(Elvidge <i>et al</i> 2007)
2010–2017	30 m	Finer Resolution Observation and Monitoring of Global Land Cover	FROM-GLC	Impervious surface	Conventional maximum likelihood classifier, the J4.8 decision tree classifier, the random forests ensemble classifier and the support vector machine	Landsat images	(Gong <i>et al</i> 2013)

of the j th pixel; $W_{l,i,d}^2$ is the weight of this convolution layer; $Bias_i^2$ is the bias; and K_1 is the size of the neighborhood.

The third convolutional layer (which contains 20 convolutional kernels with a size of 1×1 pixel) and a pooling layer with a kernel size of 51×51 pixels are combined to obtain information at the scale of urban regions. The kernel size of 51×51 pixels used in the pooling layer is determined based on the largest urban region in the world (Angel *et al* 2016). The relationship between the third convolutional layer and the pooling layer can be represented by the equations (3), (4):

$$Conv_{i,j}^3 = \sum_I^{N_0} (W_{I,i}^3 \cdot Pool_{I,j}) + Bias_i^3, \quad (3)$$

where $Conv_{i,j}^3$ and $Pool_{I,j}$ denote the DN values in the third convolution layer and the pooling layer respectively; $W_{I,i}^3$ is the weight of this convolution layer; $Bias_i^3$ is the bias

$$Pool_{I,j} = \sum_g^{K_2 \cdot K_2} Input_{I,j,g} / (K_2 \cdot K_2), \quad (4)$$

where $Input_{I,j,g}$ denotes the DN value of the g th pixel within the urban region of the j th pixel in the I th band in the input layer; and K_2 denotes the size of the urban region.

The concatenation layer is used to integrate the information obtained by the three convolutional layers, and their relationships can be represented by the equation (5):

$$Conc_{i,j} = \begin{cases} f(Conv_{i,j}^1), & i \leq 80 \\ f(Conv_{i-80,j}^2), & 80 < i \leq 120 \\ f(Conv_{i-120,j}^3), & 120 < i \leq 140 \end{cases}, \quad (5)$$

where $Conc_{i,j}$ denotes the DN value in the concatenation layer, and $f(x)$ denotes the activation function, which can be represented by the equation (6):

$$f(x) = \max(0, x). \quad (6)$$

The relationship between the concatenation layer and the output layer can be represented by the equation (7):

$$Urban_j = \begin{cases} 1, & Output_j^{urban} > Output_j^{non-urban} \\ 0, & Otherwise \end{cases}, \quad (7)$$

where $Urban_j$ denotes the class value in the output layer, in which 1 represents urban land whereas 0 represents non-urban land. $Output_j^{urban}$ and $Output_j^{non-urban}$ denote the probability that the j th pixel represents urban land or non-urban land respectively. These probabilities can be calculated using the following equations:

$$Output_j^{urban} = f\left(\sum_i^{140} (W_i^{urban} \cdot Conc_{i,j}) + Bias^{urban}\right), \quad (8)$$

$$Output_j^{non-urban} = f\left(\sum_i^{140} (W_i^{non-urban} \cdot Conc_{i,j}) + Bias^{non-urban}\right), \quad (9)$$

where W_i^{urban} and $W_i^{non-urban}$ are weights, and $Bias^{urban}$ and $Bias^{non-urban}$ are biases. The FCN is developed using the Convolutional Architecture for Fast Feature Embedding (Caffe) software platform (Jia *et al* 2014).

3.2. Calibrating the FCN

The objective of calibration is to obtain the weights used in the FCN. Essentially, calibration involves iteratively estimating these weights using optimization algorithms with the goal of minimizing the loss function. This process includes three main steps: selecting training samples, determining the loss function, and setting the optimization algorithm and iteration parameters. First, we select training samples that represent urban and non-urban land from the MOD500 data and NTL data that cover the same period. The selection of training samples can be calculated using the equation (10):

$$Train_i = \begin{cases} 1, & Mod_i = 1 \\ 0, & Mod_i = 0 \text{ and } PUL_i = 1 \\ -1, & Otherwise \end{cases}, \quad (10)$$

where $Train_i$ and Mod_i denote the class of the i th pixel in the training sample data and the MOD500 data respectively. A value of 1 denotes urban land, a value of 0 denotes non-urban land, and a value of -1 denotes the background, which is not included in the calibration to improve efficiency. PUL_i denotes the class value in a potential urban land data, which takes values of 1 (potential urban land) or 0 (not potential urban land). The pixels with DN values greater than $1 \text{ nW cm}^{-2} \text{ sr}^{-1}$ in the NTL data were recognized as potential urban land (Dou *et al* 2017).

Further, we calculate the loss function after the output layer based on the equation (11) (Jia *et al* 2014):

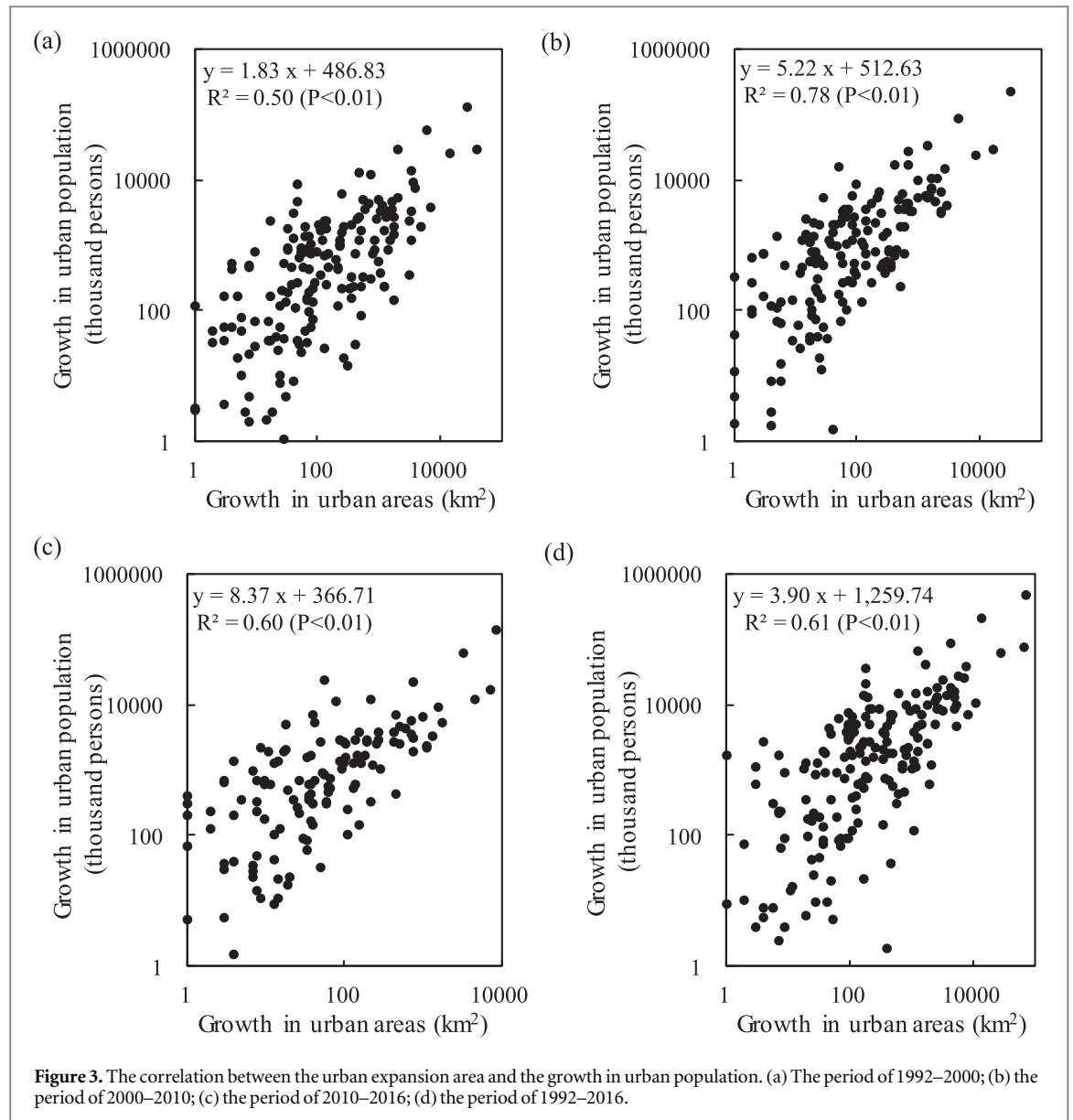
$$l(y, z) = \log \sum_j e^{z_j} - z_y, \quad (11)$$

where z denotes the inputs to the loss function; $l(y, z)$ denotes the loss function of z ; z_j denotes the result of estimating the j th class; and y denotes the class of z in the training samples.

Finally, following Long *et al* (2015), we utilize the stochastic gradient descent algorithm to perform the optimization. The iteration step size is 1×10^{-7} , and the maximum number of iterations is 1 million. The parameters of gamma and momentum both are 0.99. The weight decay is 0.0005.

3.3. Detecting global urban expansion from 1992–2016

First, we calibrate four FCNs with different remote sensing data using the Caffe deep learning platform so that the urban land at different times can be detected



effectively (Jia *et al* 2014). Specifically, the first FCN applied for detecting urban land in 1992, is calibrated using the intercalibrated DMSP-OLS NTL data. The second FCN applied for detecting urban land in 1996, is calibrated on the basis of the radiance-calibrated DMSP-OLS NTL data. The third FCN applied for detecting urban land in 2000, 2006, and 2010, is calibrated on the basis of the radiance-calibrated DMSP-OLS NTL and LST data. The fourth FCN applied for detecting urban land in 2016, is calibrated on the basis of the NPP-VIIRS NTL and LST data. All of the FCNs involve NDVI, longitude, and latitude. We then use the calibrated FCNs to extract the global urban land for 1992, 1996, 2000, 2006, 2010, and 2016, respectively. We follow this step

with the post-classification processing described below to ensure that the extracted global urban lands in different years are comparable. Because urban land has relatively high population densities, stronger NTL, and lower NDVI values, the areas of urban expansion generally show increased population densities and NTL and decreased NDVI values (Elvidge *et al* 2007, He *et al* 2014). In contrast, areas that have been transformed from urban land to non-urban land usually show decreased population densities and NTL and increased NDVI values. Therefore, we correct the extracted global urban land using the NTL, NDVI, and population densities from the HYDE dataset. The procedure can be represented by equation (12):

$$Urban_{i,j}^{Cor} = \begin{cases} 1, & (UD_{i,j}^{Pre} \neq -1 \text{ and } Urban_{i,j}^{Pre} = 1) \text{ or } (UD_{i,j}^{Post} \neq 1 \text{ and } Urban_{i,j}^{Post} = 1) \\ Urban_{i,j}, & \text{Otherwise} \end{cases}, \quad (12)$$

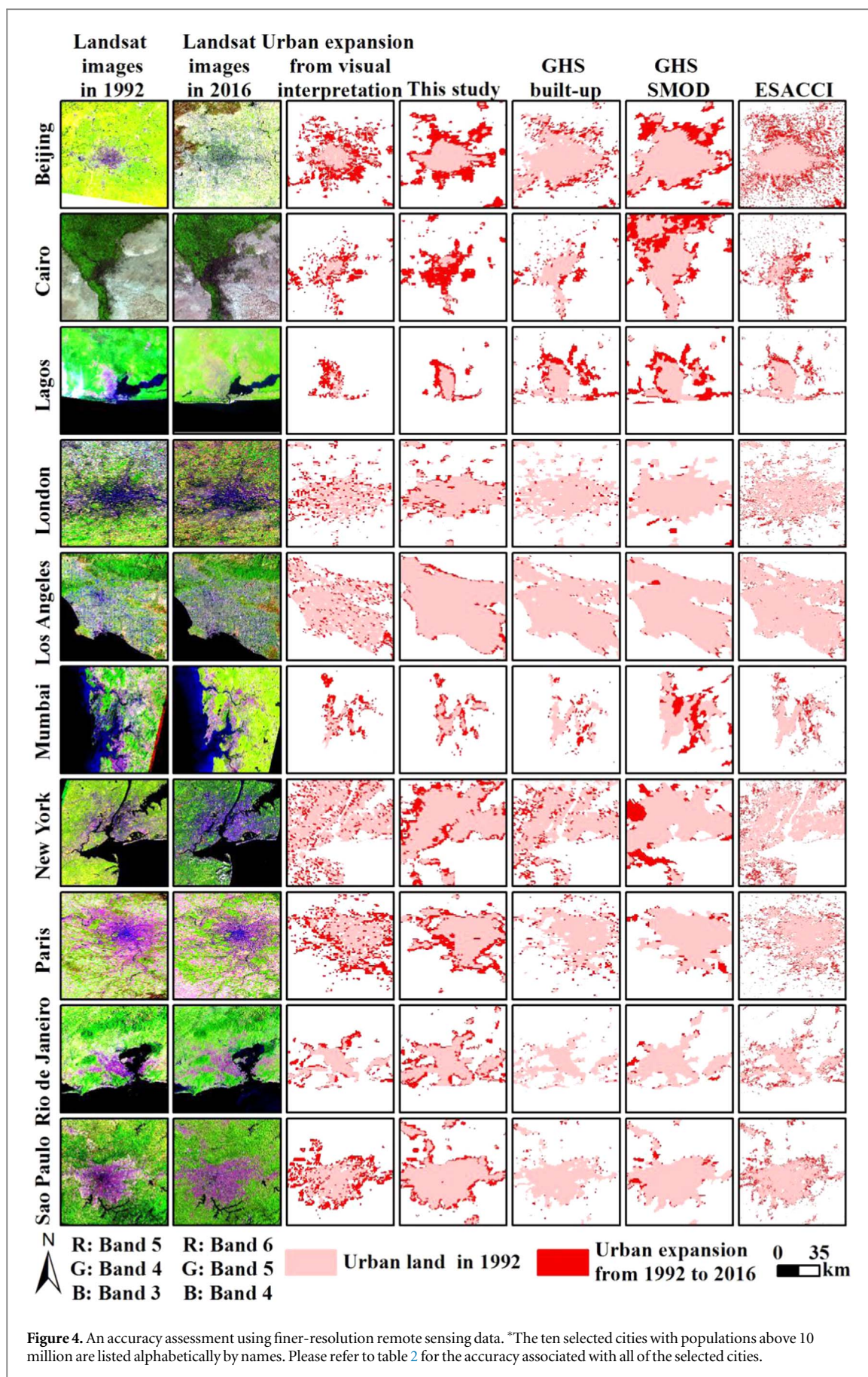
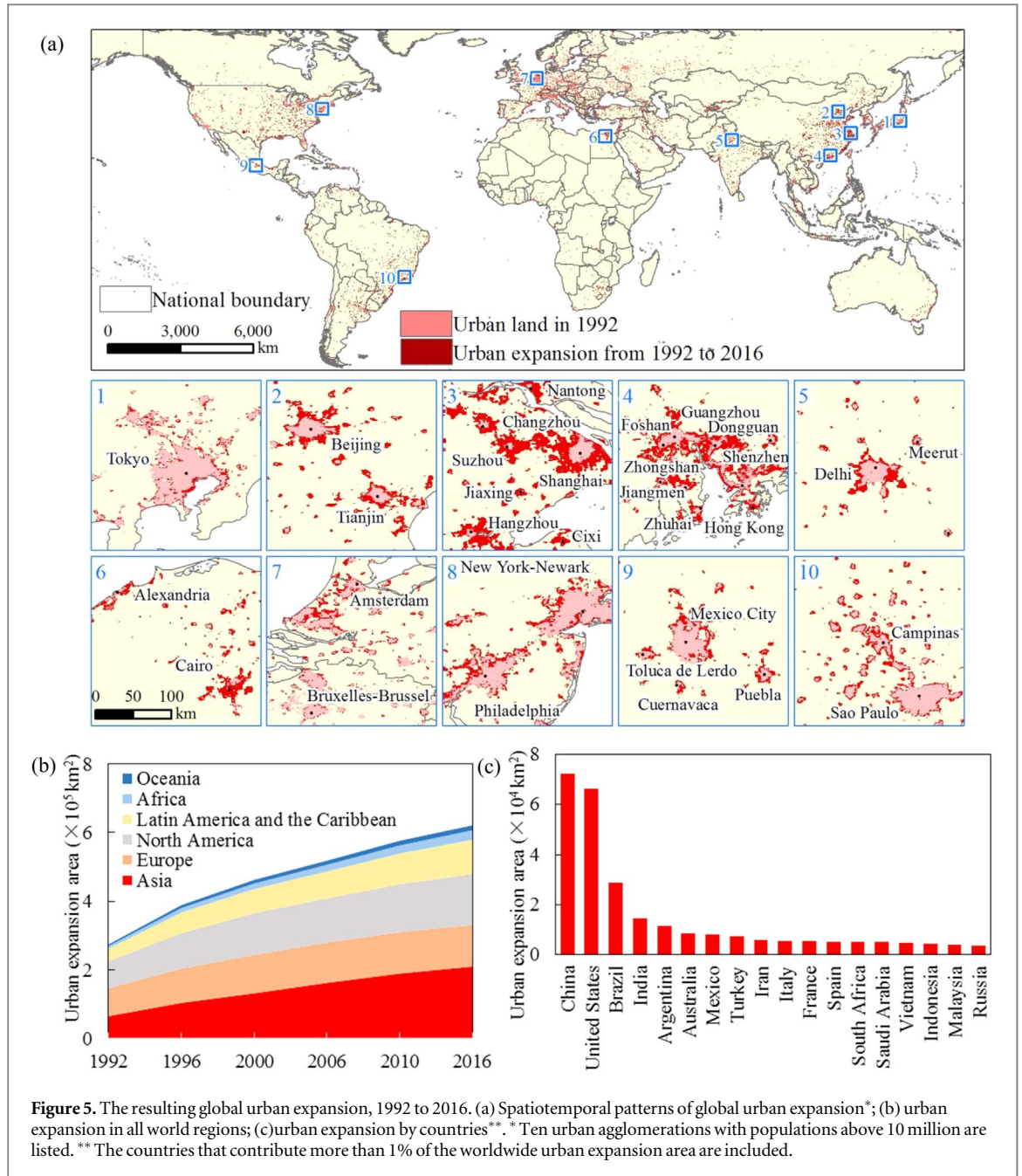


Figure 4. An accuracy assessment using finer-resolution remote sensing data. *The ten selected cities with populations above 10 million are listed alphabetically by names. Please refer to table 2 for the accuracy associated with all of the selected cities.

Table 2. An accuracy assessment of urban expansion results for the selected cities.

Continent	Country	City	Population circa 2016 (million persons)	This study				GHS built-up				GHS MOD				ESACCI				
				Kappa	OA ^a (%)	OE ^a (%)	CE ^a (%)	Kappa	OA ^a (%)	OE ^a (%)	CE ^a (%)	Kappa	OA ^a (%)	OE ^a (%)	CE ^a (%)	Kappa	OA ^a (%)	OE ^a (%)	CE ^a (%)	
Africa	Egypt	Cairo	19.12	0.51	92.10	32.87	53.67	0.51	96.63	58.80	28.23	0.48	96.19	57.41	39.07	0.30	95.85	78.70	38.67	
		Nigeria	Lagos	13.66	0.50	90.59	50.14	39.22	0.01	78.06	85.51	88.04	0.09	71.94	91.59	94.83	0.06	84.81	89.57	80.65
		Uganda	Kampala	2.01	0.41	96.36	65.82	41.94	0.33	93.61	55.70	69.96	0.09	88.99	78.48	90.09	0.37	95.27	61.39	59.33
		Rwanda	Kigali	1.29	0.78	96.16	28.57	10.00	0.45	90.82	55.56	41.67	0.08	71.95	90.48	94.87	0.47	91.32	55.56	37.78
		Zambia	Ndola	0.51	0.54	96.88	52.63	33.33	0.14	94.61	86.84	77.27	0.00	90.95	94.74	96.00	0.27	96.12	81.58	41.67
Asia	Mozambique	Beira	0.45	0.39	98.38	63.64	55.56	0.23	98.56	84.85	44.44	0.12	98.11	90.91	80.00	0.23	98.56	84.85	44.44	
		China	Beijing	21.24	0.62	93.75	41.84	24.94	0.21	89.35	82.05	55.32	0.19	87.20	78.13	68.34	0.30	89.90	74.03	48.86
	India	Mumbai	21.36	0.59	93.15	44.27	27.93	0.22	88.60	79.47	59.69	0.03	77.91	89.60	92.22	0.23	89.48	80.53	51.66	
	Vietnam	Ho Chi Minh City	7.50	0.69	88.33	20.62	26.25	0.29	80.10	75.14	24.79	0.04	66.48	76.55	73.14	0.37	81.52	66.38	24.68	
	Indonesia	Medan	2.23	0.67	94.50	41.28	14.63	0.13	88.42	88.59	63.04	0.06	81.52	96.64	95.76	0.12	88.53	89.60	62.65	
	Turkey	Malatya	0.43	0.71	97.88	28.07	26.79	0.17	96.25	89.47	40.00	0.37	95.90	66.67	53.66	0.00	96.04	100	100	
	Malaysia	Ipoh	0.75	0.58	90.38	33.52	38.89	0.38	89.68	69.78	27.63	0.42	90.31	67.03	22.08	0.39	88.91	64.84	39.05	
	Europe	France	Paris	10.93	0.48	86.60	52.35	32.12	0.22	83.79	82.16	32.11	0.19	83.39	84.83	34.56	0.11	83.10	92.09	22.92
			United Kingdom	London	10.43	0.32	93.48	69.84	57.55	0.10	93.43	92.11	71.11	0.04	93.03	95.75	84.21	0.07	93.73	95.34
		Italy	Milan	3.10	0.45	88.63	57.07	37.37	0.12	86.50	90.92	44.55	0.17	86.24	85.71	50.14	0.05	86.13	96.35	55.24
Poland		Warsaw	1.73	0.50	95.92	60.65	25.28	0.20	94.68	86.69	42.31	0.24	94.42	81.66	51.56	0.14	94.37	90.83	55.07	
Greece		Thessaloniki	0.73	0.18	76.77	64.18	71.08	0.20	86.10	85.07	28.57	0.03	82.23	94.03	78.95	0.16	84.28	85.07	54.55	
Russia	Tyumen	0.63	0.37	97.46	69.64	50.00	0.03	97.46	98.21	50.00	0.03	97.39	98.21	71.43	0.00	97.46	100	50.00		
Latin America and the Caribbean	Brazil	Sao Paulo	21.30	0.47	87.94	59.33	24.17	0.07	83.64	95.15	36.99	0.10	82.89	90.62	55.94	0.20	84.91	85.46	25.41	
		Rio de Janeiro	12.98	0.33	91.47	50.64	69.90	0.09	95.57	94.33	64.47	0.17	95.10	86.55	68.47	0.11	95.19	91.81	72.73	
	Mexico	Guadalajara	4.92	0.66	92.24	34.87	22.60	0.32	88.17	76.95	18.37	0.30	86.34	72.33	44.83	0.30	88.13	78.67	14.94	
	Guatemala	Guatemala	2.99	0.63	93.84	30.46	35.64	0.26	91.99	81.61	30.43	0.00	84.33	91.38	90.68	0.15	91.47	90.23	34.62	
	Colombia	Valledupar	0.43	0.74	99.71	34.62	15.00	0.29	99.42	80.77	37.50	0.29	99.30	76.92	60.00	0.19	99.40	88.46	40.00	
	Brazil	Palmas	0.15	0.42	96.63	26.00	68.91	0.00	98.19	100	100	0.69	98.65	12.00	42.11	0.38	98.44	72.00	36.36	
	Northern America	United States	Los Angeles	12.32	0.18	82.27	75.83	66.42	0.16	84.88	85.08	57.64	0.13	84.77	87.62	59.95	0.14	84.92	86.69	58.01
			New York	18.60	0.08	81.72	83.51	79.32	0.15	83.01	77.94	72.85	0.09	82.21	83.39	78.38	0.10	87.06	91.39	60.24
			Portland	2.03	0.59	91.00	41.61	27.95	0.25	87.71	82.38	23.36	0.21	87.29	85.23	27.27	0.21	86.91	83.56	37.58
			Philadelphia	5.60	0.28	88.62	65.48	66.80	0.20	91.11	83.32	56.93	0.16	91.09	87.28	59.15	0.11	91.62	92.46	48.30
Springfield			0.65	0.43	92.21	64.89	29.46	0.12	88.82	88.44	69.05	0.14	90.25	89.78	48.89	0.06	90.34	96.00	40.00	
Canada	Victoria	0.36	0.16	85.23	82.14	65.52	0.16	86.71	85.96	55.56	0.04	86.71	96.49	66.67	0.10	84.01	85.96	73.33		
Oceania	Australia	Sydney	4.54	0.60	94.88	37.84	36.63	0.22	93.60	85.11	32.30	0.13	92.88	90.71	56.13	0.18	93.12	87.30	48.33	
	New Zealand	Auckland	1.36	0.17	69.51	31.65	81.82	0.17	89.42	83.54	67.50	0.08	85.67	84.81	83.10	0.14	89.76	87.34	67.74	
	Fiji	Suva	0.18	0.38	81.73	59.09	40.00	0.00	78.85	100	50.00	0.00	74.04	100	100	0.00	78.85	100	50.00	
	Australia	Gold Coast	0.60	0.40	93.81	39.82	66.00	0.51	96.63	58.80	28.23	0.26	96.59	77.61	65.12	0.39	96.55	67.80	43.56	
	Average			0.47	90.89	49.85	43.02	0.20	90.13	82.54	49.70	0.15	87.42	83.27	66.99	0.19	90.47	84.47	49.67	

^a OA: overall accuracy, OE: omission error, CE: commission error.



where $Urban_{i,j}^{Cor}$ denotes the value in the corrected urban land data; i indicates the year; j indicates the pixel; $Urban_{i,j}^{Pre}$ and $Urban_{i,j}^{Post}$ denote the values in the urban land data in the years before and after the i th year, respectively. The value of 1 denotes urban, while 0 denotes non-urban. $UD_{i,j}^{Pre}$ and $UD_{i,j}^{Post}$ denote the

conversion from non-urban land to urban land; the value of -1 denotes the transformation of urban land into non-urban land; and the value of 0 denotes an uncertain conversion. $UD_{i,j}^{Pre}$ can be calculated using the following equation:

$$UD_{i,j}^{Pre} = \begin{cases} 1, & Pop_{i,j} > Pop_{i,j}^{Pre} \text{ and } NTL_{i,j} > NTL_{i,j}^{Pre} \text{ and } NDVI_{i,j} < NDVI_{i,j}^{Pre} \\ -1, & Pop_{i,j} < Pop_{i,j}^{Pre} \text{ and } NTL_{i,j} < NTL_{i,j}^{Pre} \text{ and } NDVI_{i,j} > NDVI_{i,j}^{Pre}, \\ 0, & \text{Otherwise} \end{cases} \quad (13)$$

possible conversion to urban land of the j th pixel in the previous period and the latter period of the i th year. For these quantities, the value of 1 denotes the

where $Pop_{i,j}$, $NTL_{i,j}$, and $NDVI_{i,j}$ denote the population density, NTL, and NDVI corresponding to the i th year, respectively. $Pop_{i,j}^{Pre}$, $NTL_{i,j}^{Pre}$, and $NDVI_{i,j}^{Pre}$

Table 3. The resulting global urban expansion, 1992 to 2016.

Region/country*	Urban land in 1992		Urban land in 2016		Growth in urban land from 1992 to 2016	
	Area (km ²)	Percentage**	Area (km ²)	Percentage**	Area (km ²)	Percentage***
Asia	65 629	23.90%	209 815	33.78%	144 186	41.61%
China	15 865	5.78%	88 047	14.17%	72 182	20.83%
India	8012	2.92%	22 450	3.61%	14 438	4.17%
Turkey	1622	0.59%	9066	1.46%	7444	2.15%
Iran	2905	1.06%	8721	1.40%	5816	1.68%
Saudi Arabia	1646	0.60%	6657	1.07%	5011	1.45%
Vietnam	190	0.07%	4689	0.75%	4499	1.30%
Indonesia	1685	0.61%	6076	0.98%	4391	1.27%
Malaysia	1189	0.43%	5026	0.81%	3837	1.11%
North America	78 856	28.71%	148 535	23.91%	69 679	20.11%
United States	70 704	25.74%	137 093	22.07%	66 389	19.16%
Latin America and the Caribbean	36 191	13.18%	99 376	16.00%	63 185	18.24%
Brazil	15 181	5.53%	43 998	7.08%	28 817	8.32%
Argentina	5528	2.01%	16 905	2.72%	11 377	3.28%
Mexico	5321	1.94%	13 249	2.13%	7928	2.29%
Europe	81 478	29.67%	121 339	19.53%	39 861	11.50%
Italy	7688	2.80%	13 141	2.12%	5453	1.57%
France	7706	2.81%	13 018	2.10%	5312	1.53%
Spain	2971	1.08%	8216	1.32%	5245	1.51%
Russia	21 000	7.65%	24 639	3.97%	3639	1.05%
Africa	7700	2.80%	27 597	4.44%	19 897	5.74%
South Africa	2957	1.08%	8126	1.31%	5169	1.49%
Oceania	4798	1.75%	14 481	2.33%	9683	2.79%
Australia	4412	1.61%	12 762	2.05%	8350	2.41%
The world	274 652	100.00%	621 143	100.00%	346 491	100.00%

*The countries that contribute more than 1% of the worldwide urban expansion area are included.

**Percentage of global urban land area.

***Percentage of global urban expansion area.

denote the population density, NTL, and NDVI in the year before the i th year, respectively. $UD_{i,j}^{Post}$ can be calculated using the following equation:

urban population at the national level for 1992–2000, 2000–2010, 2010–2016, and 1992–2016. The estimated urban land expansion is strongly correlated

$$UD_{i,j}^{Post} = \begin{cases} 1, & Pop_{i,j} < Pop_{i,j}^{Post} \text{ and } NTL_{i,j} < NTL_{i,j}^{Post} \text{ and } NDVI_{i,j} > NDVI_{i,j}^{Post} \\ -1, & Pop_{i,j} > Pop_{i,j}^{Post} \text{ and } NTL_{i,j} > NTL_{i,j}^{Post} \text{ and } NDVI_{i,j} < NDVI_{i,j}^{Post} \\ 0, & \text{Otherwise} \end{cases} \quad (14)$$

where $Pop_{i,j}^{Post}$, $NTL_{i,j}^{Post}$, and $NDVI_{i,j}^{Post}$ denote the population density, NTL, and NDVI in the year after the i th year, respectively. Finally, we obtain information on the global urban expansion from 1992–2016.

($R^2 \geq 0.5$) with the census data at a statistically significant level of 0.01 (figure 3).

4. Results

4.1. Accuracy assessment

We first evaluate the estimated urban expansion area resulting from this study at the national level using population census data (Sutton 2003, Zhang and Seto 2011). Using census data provided by the United Nations, we analyze the relationships between the estimated growth of urban land and the growth of

Following the procedure presented by Potere *et al* (2009), we then use finer-resolution remote sensing data (Landsat imagery with a 30 m resolution) to evaluate the estimated urban expansion (figure 4). During this process, we select a total of 34 cities as samples that represent various levels of socioeconomic conditions in different regions using the stratified sampling approach introduced by Angel *et al* (2016) based on urban population and location (figure 1). The selected cities include two cities from group 1 (with populations greater than 10 million), two cities from group 2 (with populations between 1 million–10 million), and two cities from group 3 (with populations less than 1

million) located in each of the five following regions: Asia, Africa, Europe, Northern America, and Latin America and the Caribbean. We also selected two cities from group 2 and two cities from group 3 in Oceania, where no city has a population greater than 10 million (figure 1). We then extract the areas of urban expansion between 1992–2016 for the selected cities through visual interpretation of the Landsat images as reference data. In comparing the estimated urban expansion data obtained using the FCN and the reference data derived from the Landsat imagery, we calculate the OA, the kappa coefficient, the commission error (CE), and the omission error (OE) according to Olofsson *et al* (2014) (table 2, figure 4). The assessment results in the average values of 90.9%, 0.47%, 43.0%, and 49.9% for OA, kappa, CE, and OE, respectively (table 2, figure 4). Among the selected cities, Kigali in Rwanda displays the highest kappa value of 0.78 and is followed by Valledupar in Columbia and Malatya in Turkey, which display kappa values between 0.70 and 0.75 (table 2). Six cities, including Ho Chi Minh City in Vietnam, Medan in Indonesia, and Guadalajara in Mexico, display kappa values between 0.6–0.7 (table 2). Seven cities, including Mumbai in India; Portland, Oregon in the United States; and Cairo in Egypt, display kappa values between 0.5–0.6 (table 2).

In addition, we compare the accuracy of our results with that of existing global urban expansion data with reference to Schneider *et al* (2010) and Zhou *et al* (2015). Among the six existing datasets that contain global urban expansion data (table 1), we first select the GHS built-up data, the GHS SMOD data, and the ESACCI data for comparison; these datasets have spatial resolutions and temporal coverage that are similar to those used in this study (tables 1–2, figure 4). We then assess the accuracy of these datasets using the reference data extracted from Landsat imagery for the selected cities and compare them with our results. This comparison shows that the accuracy of the results produced by this study is much higher than those of the existing datasets (table 2, figure 4). Specifically, the GHS built-up data display the average values of 90.1%, 0.20%, 49.7%, and 82.5% for OA, kappa, CE, and OE, respectively (table 2). The GHS SMOD data display the average values of 87.4%, 0.15%, 67.0%, and 83.3% for OA, kappa, CE, and OE, respectively (table 2). The ESACCI data display the average values of 90.5%, 0.19%, 49.7%, and 84.5% for OA, kappa, CE, and OE, respectively (table 2). The average OA and kappa of the results from this study are 0.4%–3.5% and 0.27–0.32 higher than those of these three global urban expansion datasets, respectively, whereas the average CE and OE obtained in this study are 6.7%–24.0% and 32.7%–34.6% lower (table 2).

4.2. Global urban expansion from 1992 to 2016

The world has experienced rapid urban expansion. The global urban land increased from 274.7 thousand km² to 621.1 thousand km²; these values correspond to an urban expansion area of 346.4 thousand km² and an annual growth rate of 3.5% (figure 5, table 3).

Asia displays the largest urban expansion area. Its urban land area has increased from 65.6 thousand km²–209.8 thousand km². These values correspond to an increase in urban area of 144.2 thousand km², which accounts for 41.6% of the global urban expansion area (figure 5(b), table 3). Among the countries in Asia, China displays the largest urban expansion area of 72.2 thousand km²; this value is 20.8% of the global urban expansion area. The urban areas in India and Turkey increased by 14.4 thousand km² and 7.4 thousand km², and these values account for 4.2% and 2.2% of the global urban expansion area, respectively. The urban expansion areas of five countries, Iran, Saudi Arabia, Vietnam, Indonesia, and Malaysia, contribute between 1%–2% of the global urban expansion area.

In Northern America, the urban land area increased by 69.7 thousand km² (from 78.9 thousand km²–148.5 thousand km²), and this increase accounts for 20.1% of the global urban expansion area (figure 5(b), table 3). In particular, the United States increased its urban land area by 66.4 thousand km², which accounts for 19.2% of the global urban expansion area. In Latin America and the Caribbean, the urban land area increased from 36.2 thousand km²–99.4 thousand km². This change corresponds to a net gain of 63.2 thousand km², which accounts for 18.2% of the global urban expansion area (figure 5(b), table 3). Within this region, Brazil, Argentina, and Mexico increased their urban land areas by 28.8 thousand km², 11.4 thousand km², and 7.9 thousand km² and account for 8.3%, 3.3%, and 2.3% of the global urban expansion area, respectively.

In Europe, the urban land area increased from 81.5 thousand km²–121.3 thousand km². This increase corresponds to an urban expansion area of 39.9 thousand km², which accounts for 11.5% of the worldwide growth (figure 5(b), table 3). Three countries in Europe, Italy, France, and Spain, increased their urban areas by between 5.0 thousand km²–5.5 thousand km², taking up approximately 1.5% of global urban expansion area. Russia expanded its urban areas by 3.6 thousand km², taking up 1.1% of global urban expansion area.

The areas of urban expansion in Africa and Oceania account for less than 10% of the worldwide growth (figure 5(b), table 3). In Africa, the urban land area grew from 7.7 thousand km² to 27.6 thousand km², an additional 19.9 thousand km², which accounts for 5.7% of the global growth. Within this region, South Africa increased its urban land area by 5.2 thousand km², which accounts for 1.5% of the global expansion. In Oceania, the urban land area increased from 4.8

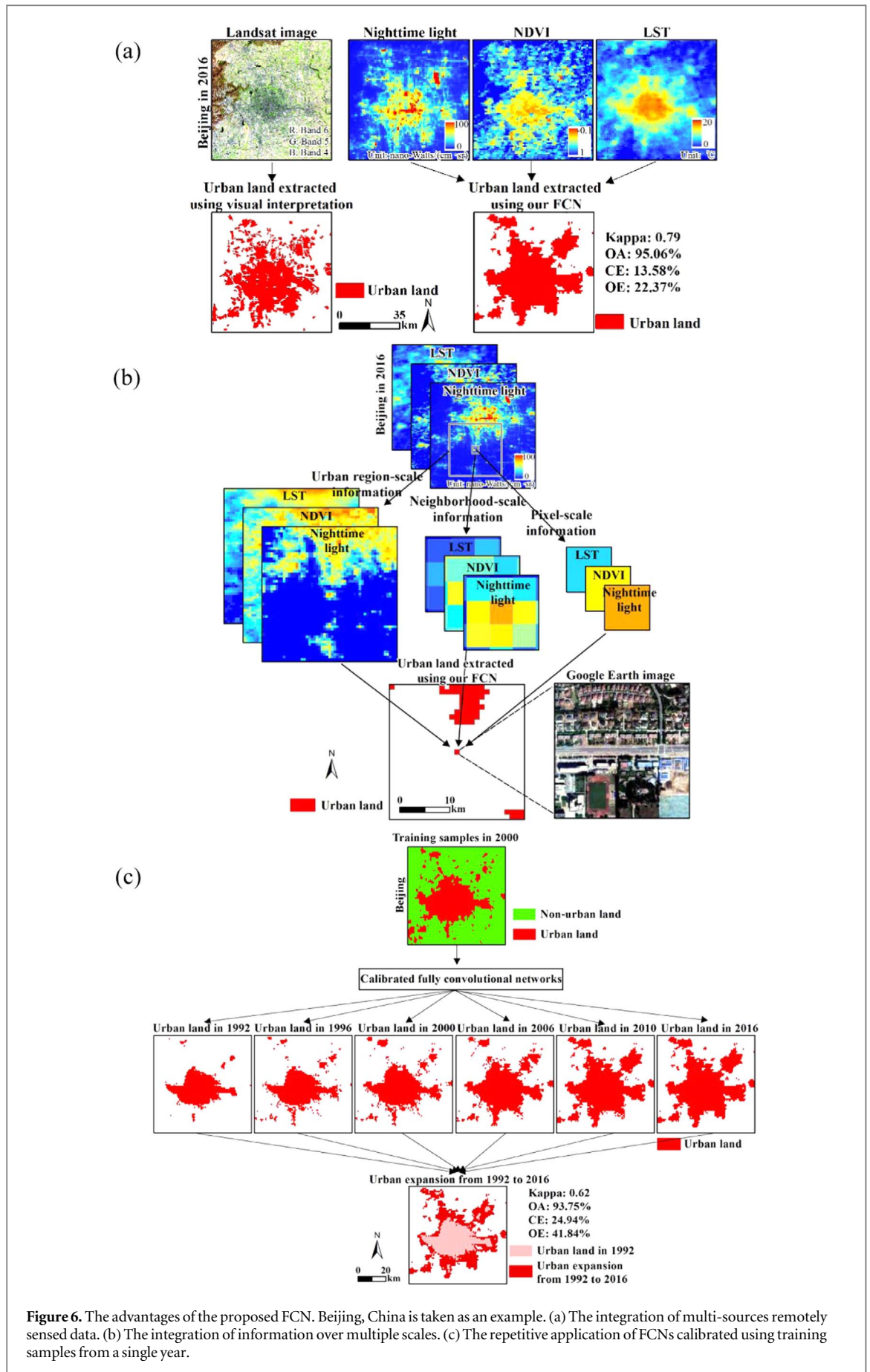


Figure 6. The advantages of the proposed FCN. Beijing, China is taken as an example. (a) The integration of multi-sources remotely sensed data. (b) The integration of information over multiple scales. (c) The repetitive application of FCNs calibrated using training samples from a single year.

thousand km²–14.5 thousand km². This change corresponds to an urban expansion area of 9.7 thousand km², which accounts for 2.8% of the worldwide growth. Within this region, Australia increased its urban land area by 8.4 thousand km², which corresponds to 2.4% of the global expansion.

5. Discussion

5.1. The proposed FCN can effectively detect global urban expansion

Presently, many classification approaches are utilized to facilitate the detection of global urban expansion (Chen *et al* 2015, Pesaresi *et al* 2016, UCL-Geomatics 2017). For example, Chen *et al* (2015) detected global urban expansion between 2000–2010 using pixel- and object-based methods with knowledge (POK). Pesaresi *et al* (2013, 2016) used a symbolic machine learning method to detect global urban expansion from 1975–2015. UCL-Geomatics (2017) applied an unsupervised classification method to study global urban expansion from 1992–2015. However, effective methods to support the study of global urban expansion are still lacking. For example, the POK method requires large amounts of manual work and time. Unsupervised classification methods and symbolic machine learning methods ignore the features of urban land over multiple scales, such as shape, texture, and background information, resulting in the confusion of urban land and barren land. In addition, the lack of training samples of historical urban land areas around the world has led to relatively low accuracy and inconsistencies among the global urban land areas extracted using classification methods.

The proposed FCN has advantages in integrating remote sensing data from multiple sources, combining features over multiple scales, and making up for the lack of historical training samples. First, FCNs inherit the abilities of artificial neural networks and permits the adaptive processing of massive data from multiple sources (LeCun *et al* 2015). The FCN used in this study employs large numbers of neurons in the convolutional layers to obtain information from different data sources, including NTL, NDVI, LST, longitude, and latitude. The fusion of various types of data is made possible through the use of a nonlinear transformation function in the activation layers. The method then selects appropriate information to effectively characterize the socioeconomic and natural attributes of urban land and provides abundant and reliable information for urban land extraction (figures 2(b) and 6(a)). Second, the FCN uses three convolutional layers and one pooling layer to obtain urban land information at the pixel, neighborhood, and urban region scales. It effectively distinguishes urban built-up areas from barren land (figures 2(b), 6(b)). Third, when calibrated using training samples at one time, the FCN can be applied repeatedly due to its

repetitive utilization of weights, which it inherits from deep learning models (Long *et al* 2015). This advantage solves the problems associated with a lack of historical training samples of urban land around the world but also improves the continuity and comparability of the extracted urban land at different times (figure 6(c)). Consequently, the proposed FCN can accurately extract urban land areas at one time and has the ability to integrate data from multiple sources and features over multiple scales (figures 6(a), (b)). For instance, the extraction of urban land in Beijing in 2016 performed using the FCN is associated with a kappa index of 0.79 and an OA of 95.1% (figures 6(a), (b)). Furthermore, we can effectively identify urban land at different times by repeatedly using the FCN. The detected urban expansion in Beijing from 1992 to 2016 is associated with a kappa index of 0.62 and an OA of 93.8% (figure 6(c)). In addition, the proposed FCN can automatically extract urban land areas from remote sensing data, which save large amounts of manual work and time. Thus, it provides an effective approach for detecting global urban expansion.

Several long-term time series of surface reflectance data are available for the study of land use dynamics. These datasets include those collected by MERIS, AVHRR, PROBA-V, and SPOT-VGT and the high-resolution radar data obtained by TerraSAR-X, TanDEM-X, and Sentinel 1, as well as crowd-sourced data, such as OpenStreetMap (Esch *et al* 2017, UCL-Geomatics 2017). These data are obtained from multiple sources and have different spatial and temporal resolutions. The proposed FCN method can easily adapt to process these datasets. Thus, it has great potential to be widely used to detect global urban land expansion using time series data.

5.2. Future perspectives

In this study, we produced a new global urban expansion dataset using the proposed FCN. This dataset has several merits over existing datasets (table 1). First, it provides adequate spatial information with 1 km resolution, which is much more precise than the HYDE dataset. Second, our dataset includes continuously comparable urban land data from 1992–2016, filling gaps in existing datasets of MGIS, GLC30 and IMPSA. Third, our dataset reveals higher accuracy than the GHS dataset, the FROM-GLC dataset and the ESACCI dataset.

In addition, the inconsistent definitions of urban land have been recognized as a primary reason for the discrepancies of existing global urban land datasets (Liu *et al* 2014). In this study, we followed Schneider *et al* (2009, 2010) and defined urban land as built-up area, i.e. the area dominated (more than 50% in cover) by non-vegetated, human-constructed elements, such as roads, buildings, runways, and industrial facilities (Liu *et al* 2014). Such definition makes our dataset

comparable with most existing datasets with similar resolution (table 1).

However, our study also has some limitations. For example, the blooming effects of NTL data and the discontinuity between the DMSP-OLS data and the NPP-VIIRS data still result in relatively high OE and CE in some cities (e.g. Los Angeles, New York, and Victoria) (table 2).

In the future, we will attempt to adjust the number of convolutional layers and the size of the convolutional kernels of our FCN using high-resolution data (Long *et al* 2015, Fu *et al* 2017) to enable the detection of global urban expansion at resolutions finer than 1 km. We will also quantify the spatiotemporal patterns of global urbanization based on the results (Seto *et al* 2011, Liu *et al* 2016a). In addition, we will use the ecological models of Carnegie-Ames-Stanford approach, Integrated Valuation of Ecosystem Services and Tradeoffs, and Service Path Attribution Networks to evaluate the impacts of global urban expansion on ecosystems (McDonald *et al* 2008, 2013, Bren d'Amour *et al* 2017).

6. Conclusions

We developed an FCN-based method to perform detection of global urban expansion. The effectiveness of this method lies in its ability to integrate remote sensing data from multiple sources, to combine features over multiple scales and to address the lack of training samples of historical urban land. Given the richness of several types of remotely sensed data, the proposed FCN has great potential to be widely used.

We obtain global urban expansion information covering the last three decades using the proposed FCN. An accuracy assessment based on census data reveals that the extracted urban land displays a strong correlation ($R^2 \geq 0.5$) with population growth at a significance level of 0.01. An accuracy assessment based on finer-resolution Landsat data indicates that our results display an average OA of 90.9% and an average kappa value of 0.47. The accuracy of our results is higher than those of existing global datasets, specifically the GHS built-up data, the GHS SMOD data, and the ESACCI data; compared to these existing datasets, the average OA and average kappa values improve by 0.4%–3.5% and 0.27–0.32, respectively.

The results show that the world has experienced large-scale urban expansion from 1992–2016. The global urban land area increased from 274.7 thousand km^2 –621.1 thousand km^2 , which is an increase of 346.4 thousand km^2 and a growth by 1.3 times. Among the six world regions, Asia displays the largest urban expansion area of 144.2 thousand km^2 and accounts for 41.6% of the worldwide growth. Among all of the countries in the world, China displays the largest urban expansion area of 72.2 thousand km^2 and accounts for 20.8% of the global increase.

Acknowledgments

This research was supported in part by the National Natural Science Foundation of China [Grant No. 41621061] and the National Basic Research Program of China [Grant No. 2014CB954302]. It was also supported by Fundamental Research Funds for the Central Universities and the projects from the State Key Laboratory of Earth Surface Processes and Resource Ecology, China.

Author contribution

Chunyang He and Zhifeng Liu designed the experiments and Zhifeng Liu carried them out. Zhifeng Liu developed the model code and performed the simulations. Chunyang He prepared the manuscript with contributions from all co-authors.

Competing interests

The authors declare that they have no conflict of interest.

Data availability

The dataset developed in this paper is freely available for noncommercial scientific applications, and the DOI for the data is <https://doi.pangaea.de/10.1594/PANGAEA.892684>.

ORCID iDs

Zhifeng Liu  <https://orcid.org/0000-0002-4087-0743>

References

- Angel S, Blei A M, Parent J, Lamson-Hall P, Sánchez N G, Civco D L, Lei R Q and Thom K 2016 *Atlas of Urban Expansion—2016 Edition, Volume 1: Areas and Densities* (New York, Nairobi, Cambridge, MA: New York University, UN-Habitat, Lincoln Institute of Land Policy)
- Angel S, Parent J, Civco D L, Blei A and Potere D 2011 The dimensions of global urban expansion: estimates and projections of all countries, 2000–2050 *Prog. Plan.* **75** 53–107
- Bren d'Amour C, Reitsma F, Baiocchi G, Barthel S, Guneralp B, Erb K H, Haberl H, Creutzig F and Seto K C 2017 Future urban land expansion and implications for global croplands *Proc. Natl. Acad. Sci. USA* **114** 8939–44
- Buyantuyev A and Wu J 2010 Urban heat islands and landscape heterogeneity: linking spatiotemporal variations in surface temperatures to land-cover and socioeconomic patterns *Landscape Ecology* **25** 17–33
- Chen J *et al* 2015 Global land cover mapping at 30 m resolution: a POK-based operational approach *ISPRS J. Photogramm. Remote Sens.* **103** 7–27
- Chen L C, Papandreou G, Kokkinos I, Murphy K and Yuille A L 2017 DeepLab: semantic image segmentation with deep convolutional nets, atrous convolution, and fully connected CRFs *IEEE Trans. Pattern Anal. Mach. Intell.* **40** 834–48

- Dou Y, Liu Z, He C and Yue H 2017 Urban land extraction using the VIIRS nighttime light data: an evaluation of three popular methods *Remote Sens.* **9** 175
- Elvidge C D, Baugh K E, Zhizhin M and Hsu F-C 2013 Why VIIRS data are superior to DMSP for mapping nighttime lights *Proc. Asia-Pac. Adv. Netw.* **35** 62–9
- Elvidge C D, Tuttle B T, Sutton P C, Baugh K E, Howard A T, Milesi C, Bhaduri B L and Nemani R 2007 Global distribution and density of constructed impervious surfaces *Sensors* **7** 1962–79
- Elvidge C D, Ziskin D, Baugh K E, Tuttle B T, Ghosh T, Pack D W, Erwin E H and Zhizhin M 2009 A fifteen year record of global natural gas flaring derived from satellite data *Energies* **2** 595–622
- Esch T, Heldens W, Hirner A, Keil M, Marconcini M, Roth A, Zeidler J, Dech S and Strano E 2017 Breaking new ground in mapping human settlements from space—the global Urban footprint *ISPRS J. Photogramm. Remote Sens.* **134** 30–42
- Fu G, Liu C, Zhou R, Sun T and Zhang Q 2017 Classification for high resolution remote sensing imagery using a fully convolutional network *Remote Sens.* **9** 498
- Gong P *et al* 2013 Finer resolution observation and monitoring of global land cover: first mapping results with landsat TM and ETM + data *Int. J. Remote Sens.* **34** 2607–54
- Grimm N B, Faeth S H, Golubiewski N E, Redman C L, Wu J, Bai X and Briggs J M 2008 Global change and the ecology of cities *Science* **319** 756–60
- He C, Liu Z, Tian J and Ma Q 2014 Urban expansion dynamics and natural habitat loss in China: a multi-scale landscape perspective *Glob. Change Biol.* **20** 2886–902
- Holben B N 1986 Characteristics of maximum-value composite images from temporal AVHRR data *Int. J. Remote Sens.* **7** 1417–34
- Jia Y, Shelhamer E, Donahue J, Karayev S, Long J, Girshick R, Guadarrama S and Darrell T 2014 *Caffe: Convolutional Architecture for Fast Feature Embedding The 22nd ACM International Conf. on Multimedia (Orlando, Florida, United States of America, November 3–7 2014)* (<https://doi.org/10.1145/2647868.2654889>)
- Klein Goldwijk K, Beusen A and Janssen P 2010 Long-term dynamic modeling of global population and built-up area in a spatially explicit way: HYDE 3.1 *The Holocene* **20** 565–73
- LeCun Y, Bengio Y and Hinton G 2015 Deep learning *Nature* **521** 436–44
- LeCun Y, Boser B, Denker J S, Henderson D, Howard R E, Hubbard W and Jackel L D 1990 Handwritten digit recognition with a back-propagation network *Proc. Advances in Neural Information Processing Systems* pp 396–404
- LeCun Y, Bottou L, Bengio Y and Haffner P 1998 Gradient-based learning applied to document recognition *Proc. IEEE* **86** 2278–324
- Liu X P, Hu G H, Chen Y M, Li X, Xu X C, Li S Y, Pei F S and Wang S J 2018 High-resolution multi-temporal mapping of global urban land using Landsat images based on the Google Earth Engine Platform *Remote Sens. Environ.* **209** 227–39
- Liu Z, He C and Wu J 2016a General spatiotemporal patterns of urbanization: an examination of 16 world cities *Sustainability* **8** 41
- Liu Z, He C and Wu J 2016b The relationship between habitat loss and fragmentation during urbanization: an empirical evaluation from 16 world cities *Plos One* **11** e0154613
- Liu Z, He C, Zhou Y and Wu J 2014 How much of the world's land has been urbanized, really? A hierarchical framework for avoiding confusion *Landscape Ecology* **29** 763–71
- Long J, Shelhamer E and Darrell T 2015 Fully convolutional networks for semantic segmentation *IEEE Trans. Pattern Anal. Mach. Intell.* **39** 640–51
- Maggiori E, Tarabalka Y, Charpiat G and Alliez P 2016 Fully convolutional neural networks for remote sensing image classification 2016 *IEEE Int. Geoscience and Remote Sensing Symp. (IGARSS)* pp 5071–4
- McDonald R I, Kareiva P and Forman R T T 2008 The implications of current and future urbanization for global protected areas and biodiversity conservation *Biol. Conservation* **141** 1695–703
- McDonald R I, Marcotullio P J and Güneralp B 2013 Urbanization and global trends in biodiversity and ecosystem services ed T Elmquist *et al Urbanization, Biodiversity and Ecosystem Services: Challenges and Opportunities* (Berlin: Springer)
- Mildrexler D J, Zhao M and Running S W 2009 Testing a MODIS global disturbance index across North America *Remote Sens. Environ.* **113** 2103–17
- Olofsson P, Foody G M, Herold M, Stehman S V, Woodcock C E and Wulder M A 2014 Good practices for estimating area and assessing accuracy of land change *Remote Sens. Environ.* **148** 42–57
- Pesaresi M, Ehrlich D, Ferri S, Florczyk A J, Freire S, Halkia S, Julea A M, Kemper T, Soille P and Syrris V 2016 Operating procedure for the production of the Global Human Settlement Layer from Landsat data of the epochs 1975, 1990, 2000, and 2014 *JRC Technical Report EUR 27741 EN* (<https://doi.org/10.2788/253582>)
- Pesaresi M *et al* 2013 A global human settlement layer from optical HR/VHR RS data: concept and first results *IEEE J. Sel. Top. Appl. Earth Obs. Remote Sens.* **6** 2102–31
- Potere D, Schneider A, Angel S and Civco D L 2009 Mapping urban areas on a global scale: which of the eight maps now available is more accurate? *Int. J. Remote Sens.* **30** 6531–58
- Schneider A, Friedl M A and Potere D 2009 A new map of global urban extent from MODIS satellite data *Environ. Res. Lett.* **4** 044003
- Schneider A, Friedl M A and Potere D 2010 Mapping global urban areas using MODIS 500 m data: new methods and datasets based on 'urban ecoregions' *Remote Sens. Environ.* **114** 1733–46
- Seto K C, Fragkias M, Güneralp B and Reilly M K 2011 A meta-analysis of global urban land expansion *Plos One* **6** e23777
- Seto K C, Güneralp B and Hutryra L R 2012 Global forecasts of urban expansion to 2030 and direct impacts on biodiversity and carbon pools *Proc. Natl Acad. Sci. USA* **109** 16083–8
- Sutton P C 2003 A scale-adjusted measure of 'Urban sprawl' using nighttime satellite imagery *Remote Sens. Environ.* **86** 353–69
- Szegedy C, Liu W, Jia Y, Sermanet P, Reed S, Anguelov D, Erhan D, Vanhoucke V and Rabinovich A 2014 *Going Deeper with Convolutions* (<https://doi.org/10.1109/CVPR.2015.7298594>)
- UCL-Geomatics 2017 Land Cover CCI—Product User Guide Version 2.0
- United Nations Department of Economic and Social Affairs 2015, Population Division: World Urbanization Prospects: The 2014 Revision, (ST/ESA/SER.A/366)
- van Vliet J, Eitelberg D A and Verburg P H 2017 A global analysis of land take in cropland areas and production displacement from urbanization *Glob. Environ. Change-Hum. Policy Dimens.* **43** 107–15
- Wu J 2014 Urban ecology and sustainability: the state-of-the-science and future directions *Landscape Urban Plan.* **125** 209–21
- Yang Y, Zhuang Y, Bi F, Shi H and Xie Y 2017 M-FCN: effective fully convolutional network-based airplane detection framework *IEEE Geosci. Remote Sens. Lett.* **14** 1293–7
- Zakšek K and Oštir K 2012 Downscaling land surface temperature for urban heat island diurnal cycle analysis *Remote Sens. Environ.* **117** 114–24
- Zhang Q and Seto K C 2011 Mapping urbanization dynamics at regional and global scales using multi-temporal DMSP/OLS nighttime light data *Remote Sens. Environ.* **115** 2320–9
- Zhou Y, Smith S J, Elvidge C D, Zhao K, Thomson A and Imhoff M 2014 A cluster-based method to map urban area from DMSP/OLS nightlights *Remote Sens. Environ.* **147** 173–85
- Zhou Y, Smith S J, Zhao K, Imhoff M, Thomson A, Bond-Lamberty B, Asrar G R, Zhang X, He C and Elvidge C D 2015 A global map of urban extent from nightlights *Environ. Res. Lett.* **10** 054011